TU Delft

Delft University of Technology

Hydrodynamic flow transition dynamics in a spacer filled filtration channel using direct numerical simulation

Qamar, Adnan; Bucs, Szilard; Picioreanu, Cristian; Vrouwenvelder, Johannes; Ghaffour, Noreddine

DOI
10.1016/j.memsci.2019.117264

Publication date
2019

Document Version
Final published version

Published in
Journal of Membrane Science

Citation (APA)
Qamar, A., Bucs, S., Picioreanu, C., Vrouwenvelder, J., & Ghaffour, N. (2019). Hydrodynamic flow transition dynamics in a spacer filled filtration channel using direct numerical simulation. *Journal of Membrane Science*, *590*, Article 117264. https://doi.org/10.1016/j.memsci.2019.117264

Important note
To cite this publication, please use the final published version (if applicable).
Please check the document version above.

Copyright
Other than for strictly personal use, it is not permitted to download, forward or distribute the text or part of it, without the consent of the author(s) and/or copyright holder(s), unless the work is under an open content license such as Creative Commons.

Takedown policy
Please contact us and provide details if you believe this document breaches copyrights.
We will remove access to the work immediately and investigate your claim.

This work is downloaded from Delft University of Technology.
For technical reasons the number of authors shown on this cover page is limited to a maximum of 10.

Journal of Membrane Science 590 (2019) 117264

Contents lists available at ScienceDirect

Journal of Membrane Science

journal homepage: www.elsevier.com/locate/memsci

Hydrodynamic flow transition dynamics in a spacer filled filtration channel using direct numerical simulation

Adnan Qamar[a], Szilard Bucs[a], Cristian Picioreanu[b], Johannes Vrouwenvelder[a], Noreddine Ghaffour[a,*]

[a] King Abdullah University of Science and Technology (KAUST), Water Desalination and Reuse Center (WDRC), Biological and Environmental Science and Engineering (BESE), Thuwal, 23955-6900, KSA, Saudi Arabia
[b] Department of Biotechnology, Faculty of Applied Sciences, Delft University of Technology, Van der Maasweg 9, 2629 HZ, Delft, the Netherlands

ARTICLE INFO

Keywords:
Desalination
Unsteady hydrodynamics
Direct numerical simulations (DNS)
Vortex dynamics
Computational fluid dynamics (CFD)
Spacer design

ABSTRACT

A vital component of spiral-wound membrane modules is the spacer mesh. It not only structurally supports the membranes but also aids in mass-transport enhancement through the membrane surface. Fundamental understanding of hydrodynamics associated with these spacer designs is critical to improve the permeate flux performance by decreasing concentration polarization and minimizing (bio)fouling, as well as minimizing the axial pressure drop. In the present study, time and space resolved Direct Numerical Simulations (DNS) were performed for a commercial spacer geometry. The spacer geometry was reconstructed by measurements using Scanning Electron Microscopy (SEM). Computations were performed for three spacer cells, allowing elimination of stream-wise periodicity that was a major bottleneck in earlier studies. The numerical solver was well checked in terms of boundary layer profiles obtained from Particle Image Velocimetry (PIV) data and with pressure measurements corresponding to various flow channel velocities. Non-dimensional computations were performed for Reynolds Numbers (Re) ranging from 73 to 375 (inlet channel velocity of 0.073–0.375 m/s) covering the flow transition dynamics regime. Results indicate that flow transition from steady to unsteady regime occurs for Re > 250. The flow transition could be primarily attributed to the interaction between vortices attached to the spacer filaments and the screw-vortex that originates along the diagonal of the spacer cells. No turbulent transition was observed even at the highest investigated velocity (Re = 375). The frequency spectra of time-varying velocity signal shows that at Re > 350 a sudden shift of frequency spectra occurs from discrete to continuous mode indicating the onset of advanced instability. Spacer design criteria in terms of maximum principal stress is also proposed, which can potentially aid in minimizing biofilm seeding.

1. Introduction

Water treatment and desalination techniques are heavily dominated by membrane processes. Spirally wound modules are not only utilized in reverse osmosis (RO) and nanofiltration (NF) processes but are also now considered for ultrafiltration (UF) and microfiltration modules with different dimensions. Spiral wound modules comprise of membrane sheets separated by feed and permeate spacers rolled on an inner perforated tube for permeate collection. The feed spacer is made of plastic wires arranged in a crossed pattern that not only supports the membrane sheets, but may also promote cross-flow water unsteadiness or turbulence through the module [1,2]. The spacers could aid in initiating flow instability (e.g., by tripping boundary layer in the channel) that results in enhanced mass transfer and thus reduced concentration polarization (CP). Although spacers may improve the permeate flux of the Spiral wound membrane module, it is also known that they promote biofouling in the system [3–6]. It has been hypothesized that regions of high shear lead to more mass transfer of particles (i.e., microbial cells or colloids) and this promotes microbial attachment and further biofilm seeding [7–9]. On the other hand, exceedingly high shear levels may also promote detachment and less fouling [4,10]. A proper balance between the rates of particle attachment and detachment would be determined by local hydrodynamics.

It has been revealed that membrane fouling follows the geometrical patterns of the spacer [7–9,11]. Earlier works on hydrodynamics and mass transport in spacer-filled channels [12–17], primarily reported average quantities in terms of correlations for friction factor and Sherwood number (in the form of $Sh = a\ Re^b Sc^c$) for various

* Corresponding author.
E-mail address: noreddine.ghaffour@kaust.edu.sa (N. Ghaffour).

https://doi.org/10.1016/j.memsci.2019.117264
Received 27 February 2019; Received in revised form 22 May 2019; Accepted 16 July 2019
Available online 19 July 2019
0376-7388/ © 2019 Elsevier B.V. All rights reserved.

commercial spacers. However, in the average sense, no noteworthy differences were observed between various spacers. Investigations primarily focused on fundamental design ([14,17,18]) highlighted that spacer orientation against the mean flow plays a critical role in pressure drop and mass transport properties.

Significant thrust in optimizing various spacer geometries for different filtration techniques has been developed by many research groups [1,19–29]. They investigated fouling by various micro-particles in feed channels [20], established correlations for solute rejection by varying the fluid properties [23,24], performed economic evaluation for different spacer configurations [1,30] and tested new spacer configurations [21,31,32], primary focusing on minimizing the CP and maximizing the permeate flux.

Direct flow visualization and measurements [33] in spacer-filled channels are still challenging. This is partly due to the small length scale (i.e., microscopic techniques are needed) and the required temporal resolution to capture fast transient flow dynamics (i.e., use of high-speed camera). Studies using Nuclear Magnetic Resonance (NMR) [9,34], Doppler measurements in Optical Coherence Tomography (OCT) [35] and Particle Image Velocimetry (PIV) [36,37] were performed. However, the methods may suffer from low spatial and temporal resolution (DOCT) or require additional micro-particles (in PIV) that have the potential to interfere with the flow or with the fouling mechanisms.

Advances in computing capabilities inspired many investigators to look into the possibilities of estimating numerically local hydrodynamics and mass transport properties. Several two-dimensional (2D) numerical investigations were performed to envisage spacer performance by assuming various idealized geometries, including unsteady or turbulent models [19,22,38–40]. More realistic performance evaluations were provided by three-dimensional (3D) simulations [4,8,10,41,42] using idealized spacer geometry, mainly assuming straight woven cylinders. Recently, numerical studies [43,44] focused on incorporating the exact spacer geometry as determined by X-ray computerized tomography (CT) is studied using hydrodynamic steady state models and revealed that the irregularities in the spacer filament diameters of commercial spacers effects pressure drop.

Limitations in terms of grid generation for 3D simulations arise in terms of spatial resolution, as the spacer geometry (like obtained from CT scans) is quite complex [45]. This becomes more prohibitive especially when performing flow transition studies. In case of known turbulent flow in a system, any appropriate turbulent closure model can be utilized. In this scenario, mesh requirements are not stringent as small turbulent scales are modeled (generally through closure equations that are solved on coarser grids) and are not captured through rigorous computations [46] by using a very fine mesh. However, for flow transition investigations, there are no closure models. As the flow regime is not known (laminar, transition or turbulent), the mesh should be sufficiently small to computationally capture relevant small flow scales (Kolmogorov scales [47]) that can lead to flow transition. For complex spacer geometry, generating fine-enough computational mesh is still challenging [48] and the generated mesh is required to satisfy Kolmogorov energy cascade law [47,49] to capture flow transition and evolving unsteadiness or turbulence.

Therefore, most of the 3D simulations are currently limited to steady state simulations or they assume turbulent state (by applying turbulent closure models [46]) on a single spacer filament cell with periodic boundary conditions in two directions [36,41]. In addition, temporal resolution in computing unsteady flows raise even more complex numerical challenges in terms of computational load. Recent investigations [2,50] have shown that fluid vorticity plays a critical role in mass transport enhancement by promoting mixing of the solute concentration field, increasing wall shear and thus reducing the mass transfer boundary layer thickness. Depending on the inlet flow rates, these vortices can either result in stationary separated zones, Von Karman shedding or transit to turbulent shedding regime [50]. In each of these regimes, the vortex dynamics is significantly different and has high potential to affect the filtration performance. Only a few studies have been dedicated to date to 3D fluid dynamics simulations in unsteady (dynamic) conditions [41,50–52], and these involved only simple (cylindrical) spacer geometry. Further, no flow transition studies exist, which can potentially identify if at a given cross-flow velocity conditions the flow is steady, unsteady or turbulent in nature inside the spacer filled channel. This information is critical as the filtration performance depend on the hydrodynamics.

This study aims to investigate flow transition behavior of commercial spacer geometries (i.e. not cylindrically idealized) inside a flow channel. DNS are performed at various Reynolds numbers in order to reveal the minimum required velocity for unsteady flow without assuming any closure models. The DNS calculations were performed for three feed spacer elements. As the size of the computational model is larger than that of a single spacer filament cell, application of periodic boundary condition in the flow direction is avoided, which is one of the major bottlenecks when performing unsteady 3D calculations [36,41]. Computations were carried out to elucidated on the unsteady hydrodynamics and associated transient vortex dynamics for Reynolds numbers (Re), covering the range applied in industrial practice.

2. Numerical setup

This section presents the numerical formulation and various parameters used in the current study. Assumptions made are in line with experiments and are physically valid in the parametric range currently investigated.

2.1. Geometry model

In the present work a commercially available non-woven Toray feed spacer with 31 mil (0.787 mm) thickness was utilized. The dimensions of this spacer were accurately obtained by Scanning Electron Microscopic (SEM) imaging, similar technique as used by Radu et al. [8]. The spacer geometry was then reconstructed using dimensions obtained by SEM projections in the x-y plane, as shown in Fig. 1. The computer-aided design (CAD) geometry reconstruction was done using SolidWorks software (Dassault Systèmes, SOLIDWORKS Corporation, Version 2016) by extruding a circular cross-section to cylindrical and conical segments of varying length. Spacer characteristic angles, the angle between the crossing filament strands and the incident flow angle, were both fixed to 90° and 45° for all the cases investigated, respectively. It has to be emphasized that keeping incident flow angle, $\alpha = 45°$, allows symmetrical orientation with respect to the incoming flow, justifying the use of a periodic condition in the span-wise direction (y-axis, normal to main flow direction).

The spacer filament cell in a physical space has dimensions of 4.38 mm × 4.38 mm × 0.78 mm, corresponding to a 31 mil spacer. The computations were however performed in a non-dimensional space, where all the spatial dimensions were scaled with respect to the characteristic length scale chosen to be the thickness of the channel (H = 0.78 mm). Therefore, in computational space the spacer filament cell dimensions correspond to 5.61 × 5.61 × 1 non-dimensional units.

The membranes were represented as walls residing on either side of the filament crossings, forming a tight flow channel. To ensure that the spacer is tightly inserted in the flow channel, no gap was left between the top/bottom membrane walls and the filament crossing, achieved by creating a spacer cavity in 0.995 non-dimensional unit thick channel. The outflow boundary was kept sufficiently far away (half-cell length) from the filament end to avoid its influence on the flow pattern inside the spacer cells. Notably, periodicity can be assumed in flow direction only in steady flow calculations. For transient calculations, periodicity can never be achieved in the mean flow direction as transient vortices generated by the spacer will be dynamically exiting the outflow boundary. All hydrodynamics quantities were sampled inside the

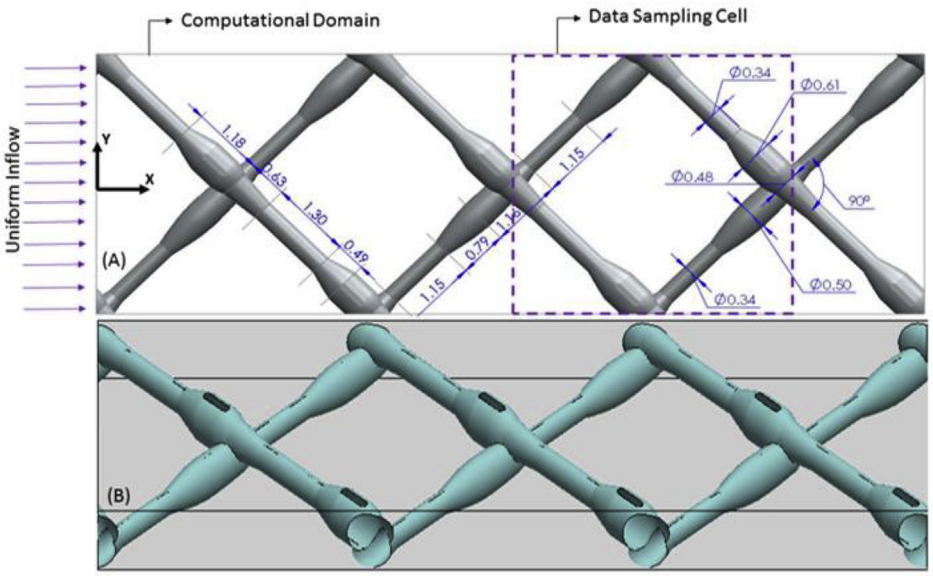

Fig. 1. Computer Aided Design (CAD) model of the reconstructed 31 mil (0.787 mm) thick feed spacer. (A) Dimensions (in mm) as obtained by Scanning Electron Microscope (SEM) images are marked in the top view of the spacer. (B) Isometric view of the feed spacer used in present computational work.

second spacer filament cell, as marked with dash lines in Fig. 1. The inflow boundary was kept sufficiently far from the data sampling cell, which aided in reducing flow entrance effects. In most of the earlier 3D transient hydrodynamic studies [41,50–52], the flow entrance effect could not be segregated, as a single spacer cell was considered owing to computational load limitations. The geometry configuration used in the present work thus better isolates both the flow entrance and outlet effects.

2.2. Flow model

In this work, DNS were performed for fluid dynamics computations [49]. Although DNS inside the spacer-filled flow channel having a rather complex geometry is computationally intensive, it has the advantage of allowing temporal and spatial flow resolution to the smallest (Kolmogorov) turbulent scales. Further, as no turbulence model is required, the solution of the direct non-dimensional Navier-Stokes equations with incompressible flow assumption was performed:

$$\nabla \cdot \mathbf{u} = 0 \tag{1}$$

$$\frac{\partial \mathbf{u}}{\partial t} + (\mathbf{u}\cdot\nabla)\mathbf{u} = -\nabla P + \frac{1}{Re}\nabla^2\mathbf{u} \tag{2}$$

where $\mathbf{u}$ is the dimensionless velocity (scaled by inlet free-stream velocity, U_o) field vector, P the dimensionless pressure (scaled by, ρU_o^2), t represents a dimensionless time (scaled by H/U_o) and ∇ the three-dimensional space gradient in dimensionless Cartesian coordinates. $Re = \rho U_0 H/\mu$ is the Reynolds number based on the average inlet velocity U_0 and channel thickness H with fluid density ρ and dynamic viscosity μ. The fluid (here water at 20 °C) was assumed to follow Newtonian behavior. Since the permeate flow (~10 μm/s) is typically very small compared to the cross-flow (in the order of 0.05% per spacer cell), the top and bottom channel walls were assumed impermeable, which allows the use of no-slip boundary condition ($\mathbf{u} = 0$). The no-slip condition was also used over the whole spacer wall surface. At the channel inlet, constant flow velocity U_0 was specified normal to the inlet face. The exit of the channel was set as an outlet flow condition [53]. In the spanwise direction, periodicity was enforced on the pressure and velocity fields, considering the spacer filament cell repetition.

2.3. Solution methodology and grid size assessment

The spatial grid resolution requirements for fluid dynamics computations using DNS are to some extent a confounding issue, especially in non-periodic 3D computations [54]. The objective in DNS calculations is not only to ensure that the solution is grid independent (i.e., minimize truncation errors associated with discretization), but also to ensure that it resolves flow structures either in steady, unsteady or turbulent state without use of any closure models [49]. For a general fluid flow, the smallest length scale depends on flow parameters and it is challenging to determine it *a priori*. Therefore, DNS mesh estimation is primarily based on experience and *posteriori* estimates, except in simple cases such as isotropic turbulence in a periodic box, where the number of grid points required to resolve the flow was theoretically calculated in the order of $Re^{2.25}$.

Grid and time-step independence tests were first performed by computing on successively refined meshes and time-steps. The number of grid points and time steps were increased such that the successive boundary layer profiles obtained from each grid overlapped, ensuring that the solution is spatially and temporally independent of discretization errors. Finally, a mesh of 2048 × 256 × 128 cells (~67 Million grid points) and a fix time step of 0.005 dimensionless time units were chosen and all reported computations were carried out on this grid and time-step resolution. The meshing of the spacer-filled flow channel was performed using an advanced cut-cell meshing approach [55]. The algorithm ensures that the majority of the discretized control volumes are hexahedrons and very few control volumes (e.g., near boundaries) are tetrahedrons in the computational domain, as shown in Fig. 2. With this meshing approach, the aspect ratio of the grid cells is easily controllable and ensures better convergence when compared to a mesh made of tetrahedrons only.

The solution of the system of Eqs. (1) and (2), along with the specified boundary conditions, was carried out on the commercial solver ANSYS Fluent (ANSYS, Inc., Version 17) that utilizes the finite-volume approach [53]. The temporal discretization was performed by using second order implicit formulation, the pressure formulation was also second order accurate, while the momentum term followed the QUICK (Quadratic Upstream Interpolation for Convective Kinematics) formulation using Fluent default relaxation factors. The pressure-velocity coupling was handled by PISO scheme.

The resulting system of discretized equations was very large,

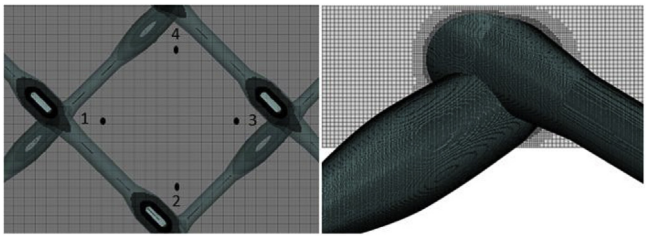

Fig. 2. (Left) Mesh generated using Cut-cell approach in the fluid domain. (Right) Zoomed mesh near the filament intersection. The mesh size in the bulk volume was 15 μm, decreasing gradually to 3 μm at the spacer surface. The control volume size in the bulk fluid was approximately $\Delta x = 15$ μm, $\Delta y = 21$ μm, $\Delta z = 7$ μm. Probe locations in the data sampling cell to gather time-dependent information (A) Location 1 (x/H = 8.84, y/H = 0, z/H = 0.5), (B) Location 2 (x/H = 11.08, y/H = −1.56, z/H = 0.5), (c) Location 3 (x/H = 12.79, y/H = 0, z/H = 0.5), and (D) Location 4 (x/H = 11.2, y/H = 1.85, z/H = 0.5), for various Reynolds numbers.

comprising 67 million grid points × 4 independent variables at each time step, with about 24000 time steps needing an average of 30 iterations per time step. Therefore all the computations were carried out on the available KAUST supercomputing facility (SHAHEEN II) [56]. For all computations, 1024 cores on Intel Haswell Processor (2 CPU socket per node, 16 cores per CPU, 2.3 GHz with 128 GB of memory per node) were utilized. For most runs 72 h of run time was sufficient for the solver to reach a steady or a periodic state. The flow state (steady or periodic) was determined by continuously monitoring velocity time signals from numerical probes as discussed in Section 4.3.

3. Experimental pressure measurement

To evaluate the DNS simulation results in the transition regime, experiments were performed to study the flow through the channel created by a 31 mil Toray commerical feed spacer. The Particle Image Velocimetry (PIV) technique was utilized to measure spatial and temporal velocities inside the channels. The experimental details and the corresponding PIV results are presented elsewhere [36].

Apart from velocity profiles, comparisons of present DNS results with experiments were also carried out for pressure drop and associated friction factor. Therefore, in the present work we also experimentally measured pressure drop at various cross-flow velocities over the spacer-filled channel in a lab-scale setup. The setup consisted of a pump (BG 2, Gather Industries, Wulfrath, Germany), mass flow controller (MINI CORI-FLOW™ M15, Bronkhorst, Ruurlo, Netherlands), flow channel with spacer, differential pressure transmitter (EndressHauser, PMD75) and a back pressure valve (EL-PRESS P–502C, Bronkhorst, Ruurlo, Netherlands). The flow channel was developed to be representative of a Spiral wound membrane element, containing amembrane and feed spacer sheet [33]. The dimension of the flow channel was 20 cm by 4 cm, and the channel height was 0.787 mm corresponding to a 31 mil thick feed spacer. The flow channel was closed with ten bolts. It was observed that the force applied to tighten the closing bolts of the flow channel impacts the differential pressure drop measurements. For this reason, pressure drop measurements were performed under four different torque values of 1, 2, 3 and 4 N m. For each tightening force pressure drop measurements were performed at 0.069, 0.099, 0.159, 0.198, 0.248, 0.297, 0.347 and 0.396 m/s cross-flow velocities.

4. Results and discussion

The present DNS computations were carried out for several Reynolds numbers, *Re* = 73, 162, 200, 250, 293, 315, 350 and 375 correlated to the equivalent linear inflow velocities of 0.073, 0.162, 0.200, 0.250, 0.293, 0.315, 0.350 and 0.375 m/s, respectively. Based on earlier work by Bucs et al. [36], this range of *Re* was selected such that the flow transition dynamics from steady to unsteady can be captured. The unsteady flow solver was first verified against the experimental results, then the flow transition dynamics and associated effects were investigated at spacer elemental level.

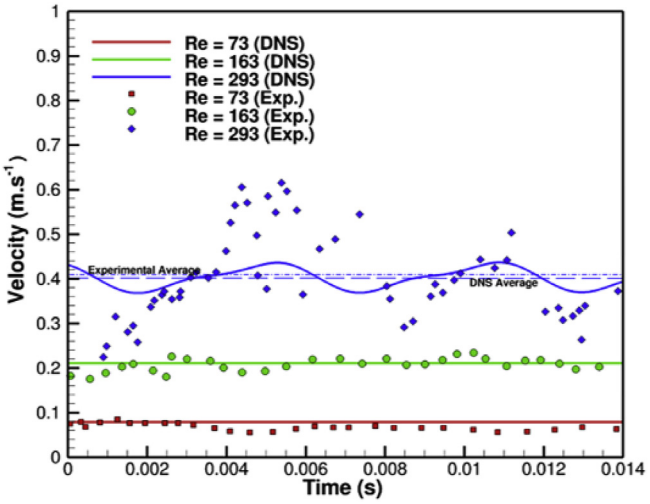

Fig. 3. Temporal comparison of the local velocity magnitude from present DNS results with experimental values measured by Bucs et al. [36] at three *Re* values and the corresponding average velocities, for a probe at $(x,y,z) = (2\text{ mm}, 2\text{ mm}, 200\ \mu\text{m})$.

4.1. Solver verification with velocity measurements

For the spatial and temporal confirmation of the numerical results we used the experimental results reported by Bucs et al. [36] obtained by particle image velocimetry (PIV). Fig. 3 shows the comparison of the instantaneous local velocity magnitude for *Re* = 73, 162 and 293, measured and calculated at probe point x = 2 mm, y = 2 mm, z = 200 μm. For the stationary flow case (*Re* = 73) results are matching well, while for the measured slightly unstable flow at *Re* = 162 the model still does not show velocity fluctuations. For the fully unsteady case (*Re* = 300), the computed velocity magnitude fluctuates with an amplitude less than that measured. The out of phase computational values in respect with the experimental values are merely a result of the stochastic nature of the flow field [57,58]. It is to be noted here that the experimental PIV data were acquired after several minutes of running the experiments. In case the flow is fully unsteady, additional benchtop factors, such as pump vibration, imperfections in spacer geometry, non-linearity in applied flow rates and flow interaction associated with flow entrance inside the flow channel could all trigger instabilities in the fluid flow. These unaccounted instabilities generally interact with the existing unsteady flow (for high Reynolds number cases) in the channel and lead to the stochastic component in flow field, as visible in the experimental data (Fig. 3, Re = 293). For steady cases, these stochastics instabilities dissipated as Reynolds number is lower (i.e. viscous effects dominates) and therefore they are only very mildly visible in time (Fig. 3, Re = 73 and 163). In numerical computations, especially for unsteady cases, the factors contributing to the stochastic nature of the flow are completely masked and, as such, no stochastic components are present. Therefore, in the unsteady regime the statistical averaging is often used to characterize the flow field. As indicated in Fig. 3, the computed average values matches well with the experimental average values.

The spatial comparison was performed by plotting the measured and computed velocity profiles along four different lines in the spacer-filled flow channel at *Re* = 162 (Fig. 4). Velocity profiles compare reasonably well, with similar profile shapes. However, the velocity magnitude at various locations in the profiles is either over or under

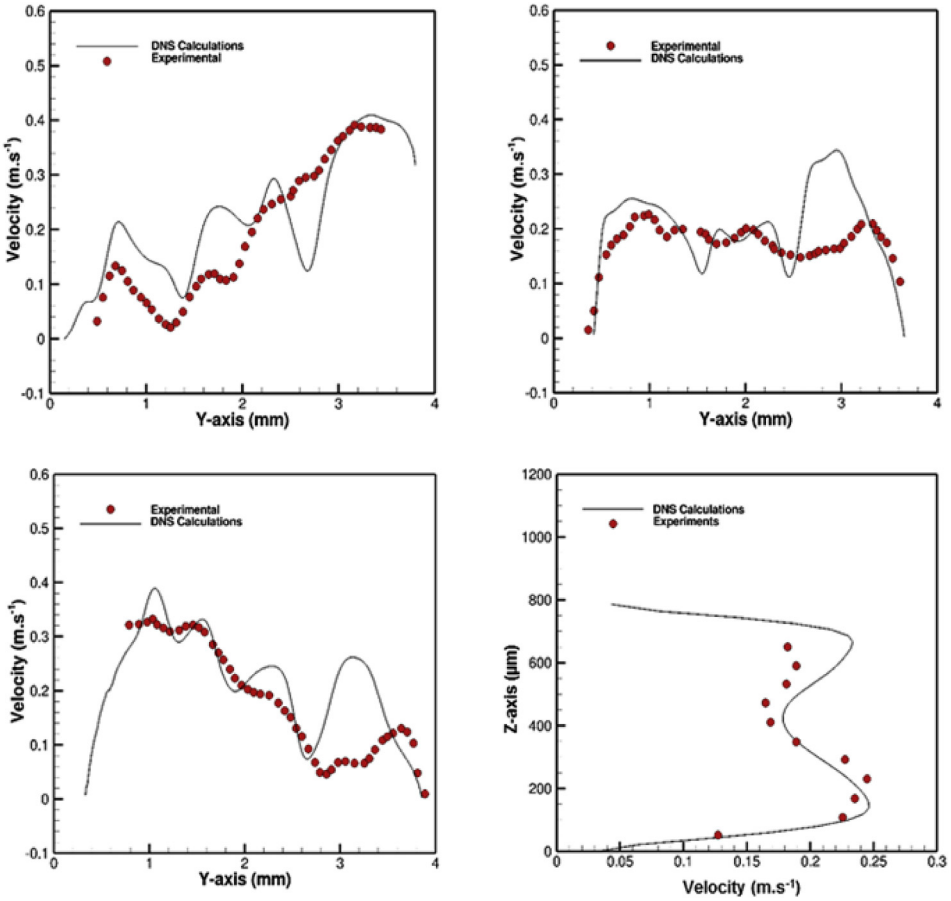

Fig. 4. Spatial comparison of local velocity magnitude by present DNS calculation with the experimental values reported by Bucs et al. [36] for Re 162: (A) along y direction at (x, z) = (2 mm, 200 µm), (B) along y direction at (x, z) = (2 mm, 400 µm), (C) along y direction at (x, z) = (2 mm, 650 µm) and (D) along z direction at (x,y) = (2.06 mm, 2.22 mm).

estimated. These differences could be attributed to various factors: (i) the modeled spacer geometry is smooth and is produced by extruding circles into smooth cone and cylinder, while actual commercial spacer geometry has many manufacturing defects and it is generally not smooth [44]; (ii) experimental errors in the time-resolved PIV measurements [59], possibly because the 3D velocity was projected on a plane or because of irregular water pumping rates; (iii) onset of flow instabilities in the experiments due to external factors (mechanical vibrations, losses by other components in experimental flow setup), while this was not observed in the simulations; (iv) other sources of error, such as possibly inexact experimental position determination or insufficient time averaging. It is important to emphasize here that in order to get better capturing of flow profiles, a much more accurate spacer geometry from advanced imaging techniques should be utilized [43,44]. In the present work, smooth spacer geometries, generated through SEM images (section 2.1) were used because creating DNS-level meshing for realistic geometries (like those obtained from Computed Tomography (CT) scans of spacers [44]) is still very challenging [48]. In addition to the local velocity profiles, the computed average pressure drop and associated quantities across the filament cell were also compared with experimental and theoretical values, and reported in the subsequent sections.

4.2. Transition dynamics – effect of varying Reynolds number

4.2.1. Flow velocity

The Reynolds numbers considered in the present numerical investigation cover the range where flow transits from steady to unsteady regime. Fig. 5 shows the instantaneous non-dimensional u-velocity component (i.e., in the main flow direction, x) for all the *Re* cases investigated. It can be observed that the computed flow is fully steady for *Re* = 73,163, 200 and 250, but it becomes unsteady for *Re* > 250, as demonstrated by the strong spatial fluctuations in velocity visible in the spacer-free area downstream the spacer. The intensity of unsteadiness increases with increasing Re and fluctuations in velocity become progressively dominant as the Re is increased (see also flow field animations in Supplementary Information video S1). For all the cases, higher u-velocity magnitudes are observed in the regions next to the conical sections of the spacer filaments cell. The low velocity region appears upstream of the filament intersections.

Supplementary video related to this article can be found at https://doi.org/10.1016/j.memsci.2019.117264.

Flow field details can be further observed in 3-D streamtrace plots on Fig. 6. The fluid stream enters the unit spacer cell past the two filaments normal to each other. The thickest cylindrical sections and the intersection of non-woven filaments form supports the membranes. This generates alternating asymmetric volumes inside the spacer cells on either side of the filament intersection. Consequently, the incoming flow stream is divided into two parts entering from both sides of the filament intersection. On both sides, most of the flow passes through the larger volumes between the spacer filament and the membrane surface. For steady flow, the fluid is transported in a woven manner along alternating filaments on either side of the filament intersection. Higher velocity magnitudes are observed in the regions above the filament where channel volume is larger compared to the side where the channel volume is smaller between the filament and the membrane.

As the Re increases in unsteady regime (Re > 250), the flow velocity increases both on top and bottom sections of the spacer element. The velocity in the smaller volume (between the filament and the membrane surface) picks up significantly enough to perturb the shear surface (i.e., the plane delimiting the region of high and low velocity) formed for low Re cases. As this shear layer gets perturbed shear instability increases and the flow transitions to unsteady regime. The boundary layer effects emerging from various geometrical elements of

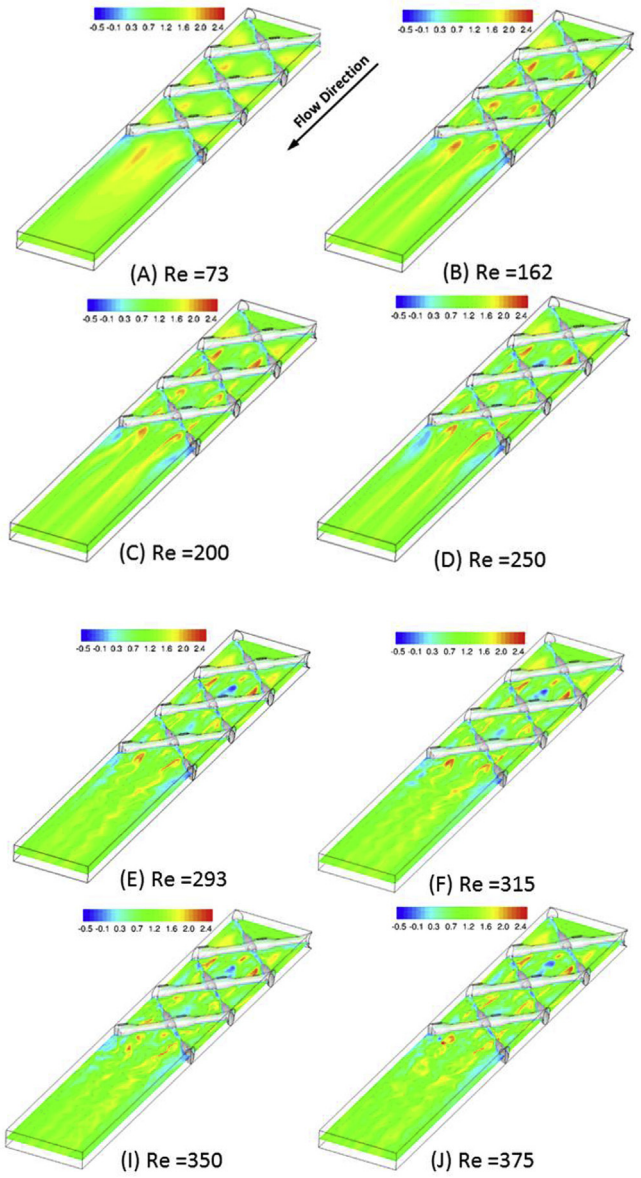

Fig. 5. Instantaneous non-dimensional u-velocity component for various Reynolds number in the x-y plane at $z/H = 0.5$. Velocity in the color scale was normalized with inlet velocity U_0. Negative u-velocity indicate a region of separated zones (dead zones). The empty space towards the end of the spacer geometry is kept, which allows application of non-periodic outlet boundary condition in the computational domain. (For interpretation of the references to color in this figure legend, the reader is referred to the Web version of this article.)

the filament (cone and cylinder) also aid in further destabilizing this shear region. As Re is further increased, separation zones start appearing in the low velocity region and ultimately vortex shedding begins, phenomenon that intensifies the flow unsteadiness. This is visible in the fluctuating streamtrace lines for unsteady case presented in Fig. 6B.

4.2.2. Vortex formation

Vortex dynamics associated with the increasing Re has also been investigated, as this is closely related to the onset of the dynamic flow and turbulence. Although determination of flow vortices, especially in three dimensions, is still mathematically ambiguous, few methods such as Q-criteria, Δ-criteria and λ2-criteria are well accepted [60]. Among these, the λ2-criterion is one of the most popular and advanced

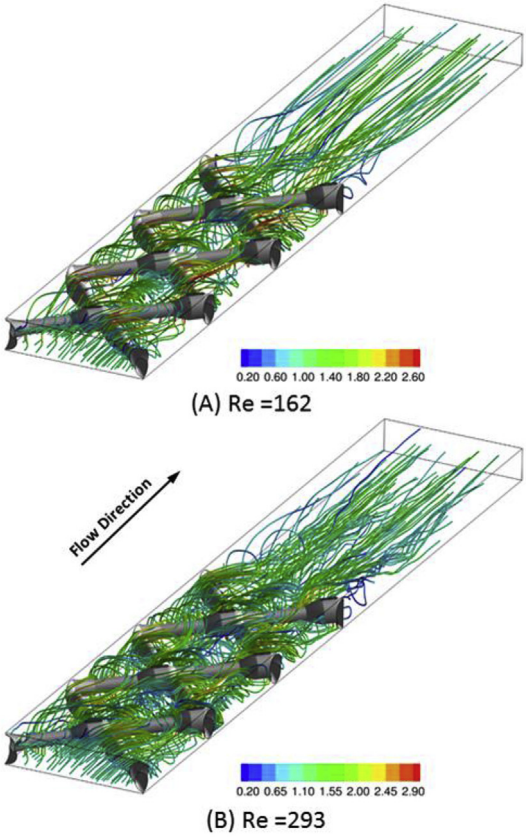

Fig. 6. Instantaneous stream traces inside the spacer filled channel contoured with velocity magnitude for (A) Re = 162 (steady regime) and (B) Re = 293 (unsteady regime). Velocity magnitude in the color scale was normalized with inlet velocity U_0. (For interpretation of the references to color in this figure legend, the reader is referred to the Web version of this article.)

methods to identify the vortex in a three-dimensional flow field. In this approach the velocity gradient tensor, D_{ij}, is decomposed into symmetric (S_{ij}) and antisymmetric (D_{ij}) parts, $D_{ij} = S_{ij} + \Omega_{ij}$, where,

$$S_{ij} = 0.5\left(\frac{\partial u_i}{\partial x_j} + \frac{\partial u_j}{\partial x_i}\right) \text{ and } \Omega_{ij} = 0.5\left(\frac{\partial u_i}{\partial x_j} - \frac{\partial u_j}{\partial x_i}\right) \quad (3)$$

A vortex is defined as a connected region with two negative eigenvalues of $S_{ij}^2 + \Omega_{ij}^2$. As the $S_{ij}^2 + \Omega_{ij}^2$ tensor is also symmetric, it has three real eigenvalues and by ordering them in $\lambda 1 \leq \lambda 2 \leq \lambda 3$ the definition becomes equivalent to requiring $\lambda 2 < 0$ [54,60]. Thus a vortex can be identified in the field by plotting iso-contours of negative λ2.

Supplementary video related to this article can be found at https://doi.org/10.1016/j.memsci.2019.117264.

The value of $\lambda 2 = -5$ was found sufficient to visualize the dominant vortex in the computational domain, as shown in Fig. 7. Small vortices that do not significantly affect the flow field are not presented and can be visualized by plotting iso-contours for values of λ2 below −5. For steady cases, the vortices are primarily attached to the filament mainly in the regions where the diameter is smaller (e.g. in the middle of filaments). Further, a large vortex also originates in the center of the filament cell with one end remaining attached to the filament intersection. As the Re increases, the attached vortices break down into subsequent smaller vortices, perturbing the steady flow and ultimately triggering the transition to unsteady regime. As the Re is increased, the fluid rotation intensifies and the large attached vortex along the diagonal of a spacer element forms a screw vortex. Remarkably, this screw-vortex has been seen in other experimental and numerical work [13,41]. Further, at much higher Re, this vortex starts shedding smaller

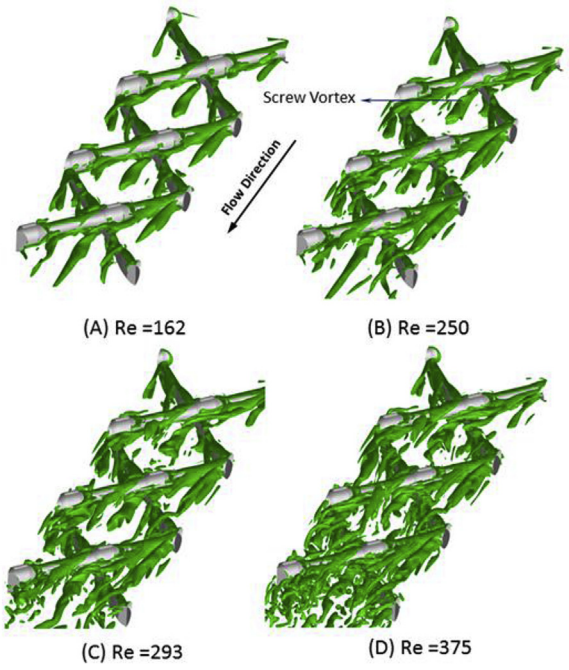

Fig. 7. Instantaneous iso-contours of vortex criterion $\lambda 2 = -5$ for spacer filled channel at (A) Re = 162, (B) Re = 250, (C) Re = 293 and (D) Re = 375. The iso-contours of $\lambda 2 = -5$ sufficiently isolate all major attached vortices appearing in the flow field at various Reynolds numbers. The arrows point to the screw vortex.

vortices from the extreme end. We hypothesize that the transition of unsteady flow to turbulent regime occurs due to shedding associated with the screw-vortex at higher Re.

Vorticity is a measure defining the fluid volume rotation. Particularly, the vorticity in the long span-wise direction (here, y-direction) primarily contributes to the vortex breakdown. Fig. 8 shows y-vorticity contours along two slices (y/H = 1 and y/H = 2) extracted from the computation domain in x-z plane. High vorticity magnitude regions start attached to the spacer filament at low Re, while these vortices start shedding as the Re is increased (see also Supplementary

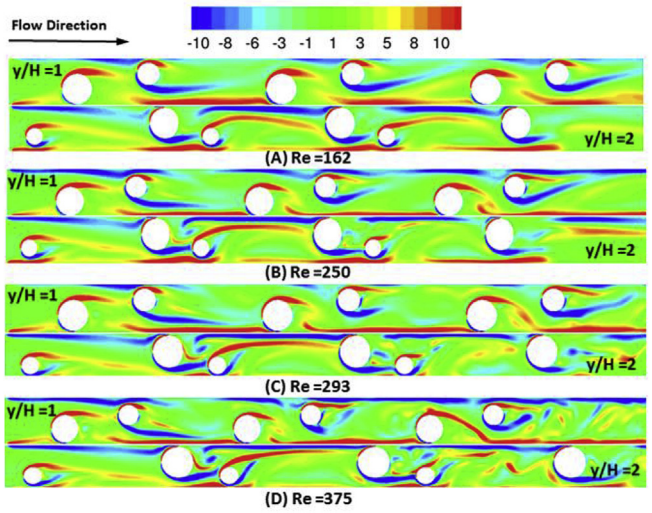

Fig. 8. Instantaneous non-dimensional y-vorticity contours for (A) Re = 162, (B) Re = 250, (C) Re = 293 and (D) Re = 375, in two sections at different y/H plane along the cell width. Increasing vorticity results in onset of unsteadiness in the spacer filled channel. Animations of the unsteady flow y-vorticity field are found in Supplementary Information videos S1 and S2.

Information videos S2 and S3). The onset of wake instability in flows behind cylindrical objects is well understood and has been found to be a manifestation of Hopf bifurcation [61] associated with span-wise vorticity component [62]. As the vorticity increases at larger Re, the rotation rate increases, which results in an instability that twists the attached vortex (Fig. 7B,C,D), which ultimately starts shedding and leads to unsteady flow and turbulence transition at even higher Re.

Supplementary video related to this article can be found at https://doi.org/10.1016/j.memsci.2019.117264.

4.2.3. Entrance effects

The present DNS study also highlights the flow entrance effects. As the flow enters the channel with constant velocity, it requires a certain length to develop a steady boundary layer profile, which is referred to as entrance length. For channels with circular cross-section, the entrance length region is well correlated with *Re* in the laminar regime ($L_{en} = 0.05\ Re\ D_h$, with L_{en} is the entrance length and D_h is the hydraulic diameter), while for a turbulent flow $L_{en} = 1.36\ Re^{0.25} D_h$, it is normally much shorter than in laminar regime [63]. However, for the spacer filled channel, this length is hard to estimate as the spacer trips down the incoming boundary layer. To allow capturing the flow dynamics in this region, more than one spacer cell had to be used in the present work. Fig. 8 clearly indicates that for all applied *Re* the flow in the entrance region remained steady in nature (steady flow region clearly visible in Supplementary Information videos S1, S2 and S3). As *Re* was increased, this region became shorter and unsteadiness moved toward the channel inlet.

4.3. Frequency spectra from steady to unsteady regime

The analysis of vortex dynamics was further performed in the frequency domain by using Fast Fourier Transform (FFT) [64]. FFT allows to detect any change in the vortex dynamics occurring due to the change in flow parameters. Numerical probes were used to collect temporal velocity data dominated by stochastic fluctuations at several locations (Fig. 9) inside the data sampling spacer cell. A triple-decomposition of these time signals at different locations, as shown in Fig. 9, was performed to analyze the flow transition from steady to unsteady or turbulent regime. The triple-decomposition of time signal is given by

$$\varphi(\mathbf{x}, t) = \bar{\varphi}(\mathbf{x}) + \varphi^*(\mathbf{x}, t) + \varphi'(\mathbf{x}, t) \tag{4}$$

where $\varphi(\mathbf{x}, t)$ is the flow variable instantaneous value, $\bar{\varphi}(\mathbf{x})$ is the time average, $\varphi^*(\mathbf{x}, t)$ is the coherent component due to large scale vortex shedding, and $\varphi'(\mathbf{x}, t)$ is the stochastic turbulent fluctuation component. Each component can be computed for the instantaneous probe $\varphi(\mathbf{x}, t)$ as:

$$\bar{\varphi}(\mathbf{x}) = \frac{1}{t_f - t_0} \int_{t_0}^{t_f} \varphi(\mathbf{x}, t) dt \tag{5}$$

$$\varphi^*(\mathbf{x}, t) = \frac{1}{n} \sum_{i=0}^{n} \varphi(\mathbf{x}, t + i \cdot T) - \bar{\varphi}(\mathbf{x}) \tag{6}$$

$$\varphi'(\mathbf{x}, t) = \varphi(\mathbf{x}, t) - \bar{\varphi}(\mathbf{x}) - \varphi^*(\mathbf{x}, t) \tag{7}$$

where $t_f - t_0$ is the total computation time, T is the vortex shedding period (determined by performing the FFT method). For all the cases investigated, the stochastic component was found to be zero, indicating that there was no turbulent transition for none of the investigated cases.

The Strouhal number ($St = H/tU_o$) variation of velocity magnitude computed at various locations in the spacer cell is presented in Fig. 9. It is evident that for the lower *Re* regime ($Re < 250$), the velocity signal should be uniform, in agreement also with measurements of Bucs et al. [36] (Re 73 and 162). For $Re > 250$, the velocity signal becomes unsteady with the amplitudes of velocity fluctuation varying with position in the spacer cell. Upstream a filament intersection (location 3, Fig. 9C),

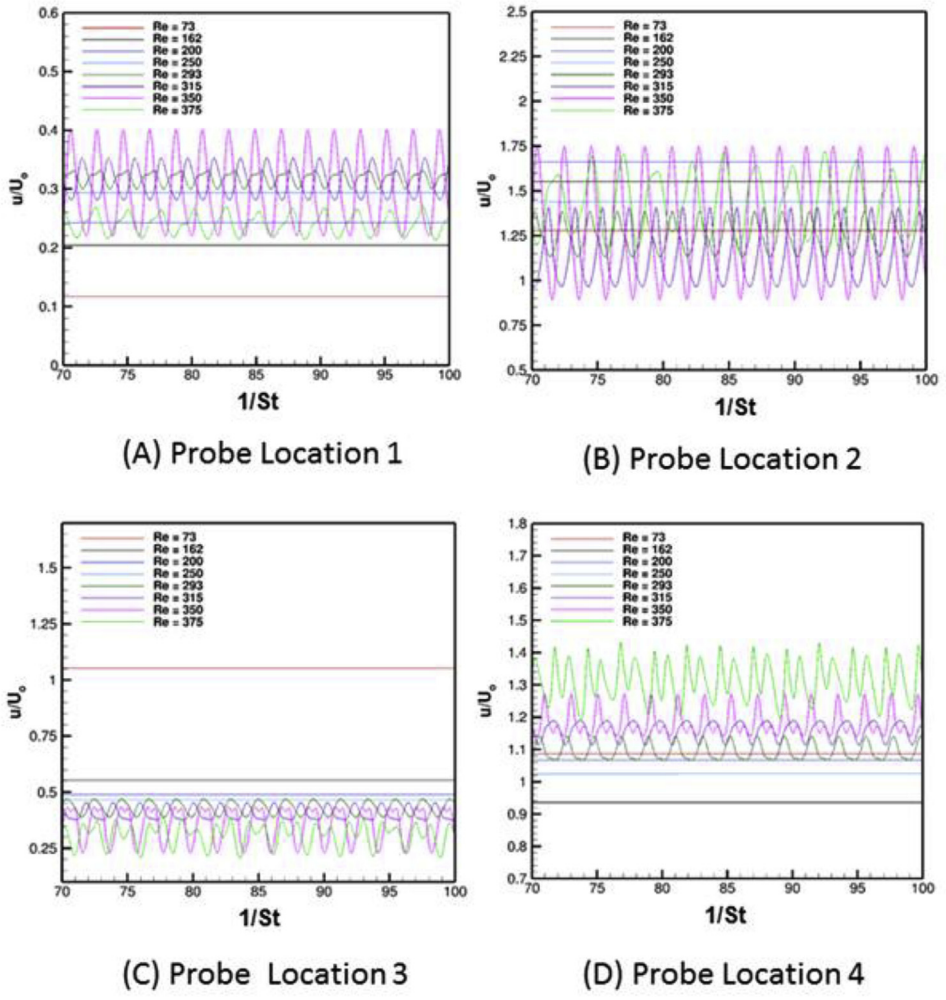

Fig. 9. Strouhal number (St = H/tU$_o$) dependency of velocity magnitude signal at four numerical probes: (A) Location 1 (x/H = 8.84, y/H = 0, z/H = 0.5), (B) Location 2 (x/H = 11.08, y/H = −1.56, z/H = 0.5), (c) Location 3 (x/H = 12.79, y/H = 0, z/H = 0.5), and (D) Location 4 (x/H = 11.2, y/H = 1.85, z/H = 0.5), for various Reynolds numbers. Both time and velocity were presented in as scaled, non-dimensional, values.

minimal velocity amplitude fluctuations were observed, whereas the maximum fluctuation amplitudes occurred at locations lateral to the filament intersections (location 4, Fig. 9D; location 2, Fig. 9B).

Frequency spectra analysis was also carried out by performing FFT of the velocity-time signal at two locations (Location 4 (x/H = 11.2, y/H = 1.85, z/H = 0.5), and Location 5 (x/H = 11.08, y/H = 0, z/H = 0.5)), as shown in Fig. 10. The frequency spectra analysis (FFT) transforms the time signal into frequency domain, which clearly helps in identifying the level of unsteadiness in the computational domain at a particular location. This analysis also provides vortex shedding frequency and indicates which frequency dominates the vortex shedding and ultimately aids in understanding flow transition phenomena. At both locations, for Re < 250 (steady regime) no significant amplitude peak with large energy content was observed, indicating flow uniformity. Further, as the Re is increased beyond 250, dominant frequencies start to appear in subharmonics manner, indicating a Von-Karman vortex shedding regime [61]. For the case of Re = 293, 315 and 350, the dominant frequency is ~0.5 while the second subharmonic dominant frequency is ~1 (Fig. 10 A and B). The highest frequency can be attributed to the shedding of the screw-vortex, whereas the second highest frequency belongs to the vortex attached to the cylindrical filament. As the flow velocity increases, the second dominant frequency starts catching up in amplitude with respect to the first dominant frequency. At Re = 350 the screw-vortex and the vortex attached to the spacer filament have almost equal strength and both influence the flow field equally.

As the Re is further increased, the frequency spectrum of velocity is no longer discrete, but quickly shifts to a continuous spectrum (Fig. 10). This potentially indicates that a Hopf-bifurcation type of instability does not initiate the flow transition (as usually seen in bluff body cases [54,61,65]), but rather an advanced level of instability occurs, which quickly transforms the discrete frequency spectrum into a more continuous type. Possibly, breaking down of bigger vortices follows a kinetic energy cascading mechanism [49]. Furthermore, for Re = 375 the energy content of vortices attached to the filament becomes dominant and dictates the vortex breakdown process. This trend is also very well captured in the λ2 iso-contours (Fig. 7C,D), which are representative of the phenomena highlighted by the frequency spectra.

4.4. Axial pressure drop variation with Reynolds number

The pressure drop over the spacer length is an important characteristic of the spacer design determining its performance in terms of pumping energy requirements. A higher pressure drop along the module means more power input, therefore, a lower pressure drop is desirable. For comparison with the available results in the literature, the average fluid velocity (U_o) was corrected for porosity (ϵ) of the spacer-filled channel, obtaining the effective velocity $U_{eff} = U_o/\epsilon$. The channel porosity was calculated as $\varepsilon = 1 - V_{sp}/V_{tot}$, where V_{sp} and V_{tot} are the volume of spacer and the total volume including spacer and

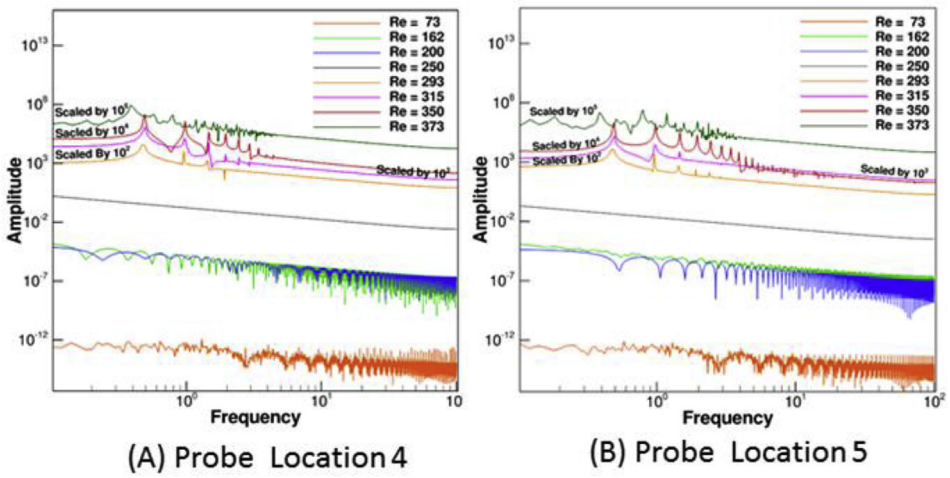

Fig. 10. Frequency spectra of the velocity magnitude at two probes: (A) Location 4 (x/H = 11.2, y/H = 1.85, z/H = 0.5), and (B) Location 5 (x/H = 11.08, y/H = 0, z/H = 0.5), for various Reynolds numbers. For better representation, the FFT amplitude was appropriately scaled as marked.

liquid, respectively. The associated drag characteristics of the spacer were investigated using the Darcy friction factor [15], $f = 2\Delta P\ d_h/(\rho\ L\ U_{eff}^2)$. Here, ΔP represents the pressure drop for a length L and d_h is the hydraulic diameter defined as:

$$d_h = \frac{4(V_{tot} - V_{sp})}{A_w} = \frac{4\ V_{tot}\ \varepsilon}{A_m + A_{sp}} \tag{8}$$

where A_w, A_m and A_{sp} represent the wetted area, membrane surface area, and spacer surface area, respectively.

For unsteady cases, the average pressure drop was calculated by sampling the instantaneous pressure field across the spacer filament over the vortex shedding cycle, as given by Eq. (5). Fig. 11 shows the variation of average pressure gradient with the effective fluid velocity in the channel, obtained by present DNS calculation and compared with data obtained from experiments by varying the torque on screw head of the flow cell cover. Overall, a non-linear, close to quadratic behavior ($\Delta P/L \sim U_{eff}^{1.75}$) was observed for the pressure drop calculated by DNS. At low velocity (low Re), the behavior is strictly quadratic following the Bernoulli's law. However, as the flow transition occurs, the pressure gradient deviates from the quadratic behavior, probably due to the onset of intermittent vortex breakdown. For unsteady cases the DNS values deviate less than 3% from the measurements. For steady cases and the highest torque value (Torque 4), the experimental measurement of pressure drop was found to deviate by 7% compared to the average DNS pressure drop. The torque on flow-cell screws basically controls the height of the filtration channel. It was found that a few micrometers difference in channel height could already alter significantly the pressure drop, due to changes in hydrodynamics. Moreover, if the membrane walls are not tightly placed on top of the spacer, flow is allowed over the filament junctions, which minimizes the unsteadiness created by spacer filament. This reduces the pressure drop at a given Reynolds for higher torque values. As the level of unsteadiness is more prominent for faster flows, this effect is more significantly observed for higher Re cases, Fig. 11A, as also indicated by Haaksman et al. [43].

The friction factor being a non-dimensional quantity provides insight into the drag characteristics of the spacer (i.e. fluid force exerted on spacers and solid walls in the feed flow direction). As visible in Fig. 11B the DNS values of friction factor decrease with increasing Re according to $f \sim Re^{-0.247}$. The value is similar to correlations available in the literature [15,41], while the differences could be attributed to the various cross-sectional shape, orientation, and size of spacer filament used in various studies.

4.5. Wall shear variation with Reynolds number

Crossflow pressure drop is an important indicator of the power consumption by the separation process, especially when the fouling significantly increases in the channel pressure drop [66]. However, flux performance and associated fouling characteristics are typically gauged by the amount of wall shear produced by the spacer. From design consideration, it would be optimal to produce just enough surface shear

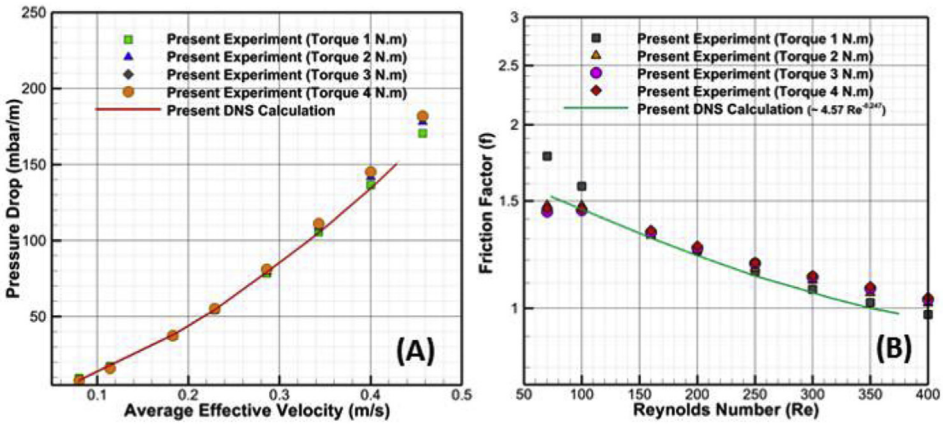

Fig. 11. Comparisons between computational and experimental results by varying torque on the screws of the flow cell cover, Torque 1, 2, 3 and 4 N m. (A) Pressure gradient per unit length at different average effective velocities, and (B) Friction factor for the flow in the spacer-filled channel as a function of Reynolds number.

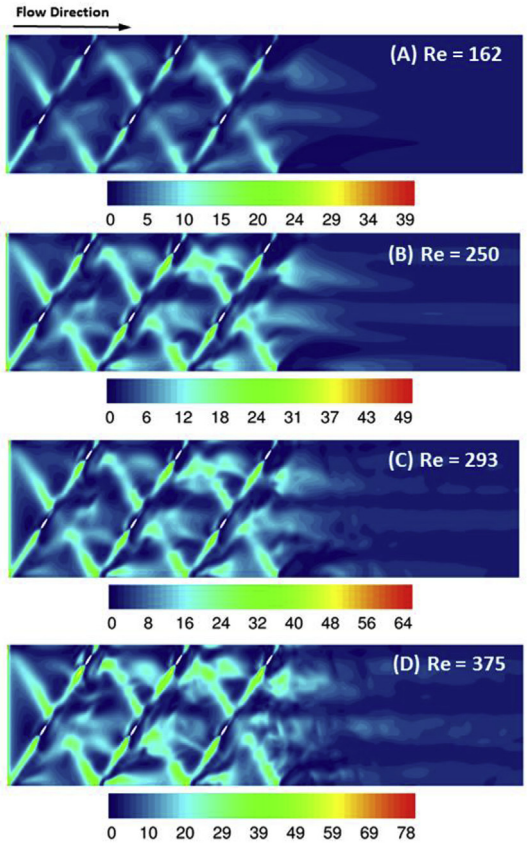

Fig. 12. Instantaneous contours of non-dimensional wall shear stress on bottom wall for (A) Re = 162, (B) Re = 250, (C) Re = 293, and (D) Re = 375.

to minimize the concentration polarization and the biofouling. Fig. 12 shows distributions of the instantaneous shear stress magnitude on one of the flow channel walls ("bottom"). Since the spacer geometry is non-woven, the wall shear stress is slightly different on top and bottom membrane walls, however, the order of magnitude and location of high shear regions are similar. For all Re investigated, high wall shear attained the highest values between the wall and the spacer filament, and the lowest values were downstream of the filament intersection, in agreement with previous studies [8,10].

For laminar flows the vortices formed behind the filament are attached and therefore the fluid stream passing over and under the filament produces more shear on the membrane surface, as seen in Fig. 12 (A, B). The transitional regimes are dominated by parallel and oblique shedding with prevalent vortex breakdown at larger Re. The breakdown of the large attached vortices allows the small vortices to enter the narrow space between the spacer and wall, thus tripping the boundary layer in that region and leading to an increase in the wall shear region as depicted in Fig. 12C,D for higher Re. The result is an intermittent and chaotic vortex dynamics, which cleans the membrane surface more efficiently than the flow in stationary regime. Vortex formation thus potentially mitigates fouling and concentration polarization.

4.6. Potential biofouling regimes

The chemical and microbiological compositions of the feed flow clearly influence the biofouling process. However, bacterial attachment and subsequent growth are also driven by the flow patterns. Although the higher and fluctuating wall shear stress is critical in minimizing the concentration polarization of solutes separated in RO and in promoting the foulant removal, high fluid stress values (like those seen under or on the spacer filaments) would promote biofilm seeding as well [67]. Therefore, from spacer design considerations, achieving an optimal balance between wall shear and maximum shear stress should be the key design goal [68]. Previous studies [7,9] have shown that biofouling in a filtration system mostly starts on the spacers from where it has potential to migrates on the membrane surface. It is therefore relevant to reveal the high fluid stress regions that could potentially serve as location for initial growth of the biofilm on spacers. The determination of maximum shear stress was achieved by computing the three-dimensional principal shear stress of the fluid. From the fluid stress tensor τ_{ij},

$$\tau_{ij} = -p\delta_{ij} + \mu\left(\frac{\partial u_i}{\partial x_j} + \frac{\partial u_j}{\partial x_i}\right) \tag{9}$$

with μ the kinematic viscosity and δ_{ij} the Kronecker delta, the three-dimensional principal stress is obtained by solving the eigenvalue problem,

$$(\tau_{ij} - \sigma\delta_{ij})n_j = 0 \tag{10}$$

where σ is the eigenvalue and n_j are the associate eigenvectors. The maximum shear stress is then given by:

$$\tau_{\max} = \frac{1}{2}(\sigma_1 - \sigma_3) \tag{11}$$

Fig. 13 shows the iso-contours of principal maximum shear stress at different Re values. Contours clearly indicate that maximum shear stress regions are along the spacer filaments. In fact, other studies [7–9] have indicated the high biomass attachment in these regions for similar non-woven spacers. As Re increases the magnitude of the principal shear stress increases too, with clear reduction in surface area affected by high shear. This potentially indicates that for higher Re, initial biofouling would be possible in a smaller area compared to low Re.

5. Conclusions

In this study, numerical simulations of fluid water flow in a channel filled with 34 mil thick commercial feed spacer were extensively performed to investigate the flow transition and its associated hydrodynamics. The numerical solution was checked using velocity profiles determined by Particle Image Velocimetry and by performing pressure

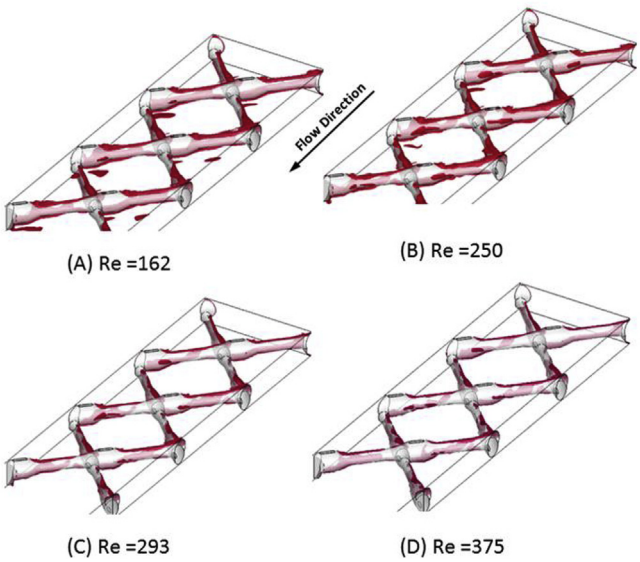

Fig. 13. Instantaneous iso-contours of principal shear stress, displayed as red surfaces. The maximum non-dimensional values of the principal shear stress (PS_{max}) are plotted for Re = 162 (PS_{max} = 28), Re = 250 (PS_{max} = 30), Re = 293 (PS_{max} = 32) and Re = 375 (PS_{max} = 35). (For interpretation of the references to color in this figure legend, the reader is referred to the Web version of this article.)

drop experiments. Pressure drop was found to vary in a quadratic manner at low effective channel velocity, whereas deviation from quadratic behavior is observed as effective velocity is increased. Flow transition to unsteady state (i.e. vortex shedding regime) begins for Re > 250 and later for Re > 350 the shedding cycle exhibits transition from a discrete shedding phase to continuous shedding (i.e., chaotic shedding marking the beginning of turbulence) as seen in the frequency spectra analysis. In addition, iso-contours of principal shear-stress provided a spatial map of potential regions where biofouling could originate.

From the present work, it appears that at the typical feed flow velocity of 0.162 m/s (Re = 162), the flow is steady in nature, as also seen in PIV experiments. This implies that the minimization of concentration polarization cannot be efficiently achieved using this non-woven spacer design. An alternative would be to operate the membrane separation process at higher velocity, which would involve larger energy consumption and may not be sufficient. Thus, future efforts should focus on designing spacers that can produce early flow transition, and by this substantially reducing the concentration polarization and therefore improving the permeate flux.

Acknowledgements

The research reported in this paper was supported by funding from King Abdullah University of Science and Technology (KAUST), Saudi Arabia. The authors also like to thank KAUST Supercomputing Laboratory (KSL) team for space allocation and technical support for solver porting, testing and scaling studies.

References

[1] A.R. Da Costa, A.G. Fane, D.E. Wiley, Spacer characterization and pressure drop modelling in spacer-filled channels for ultrafiltration, J. Membr. Sci. 87 (1994) 79–98.
[2] A.H. Haidari, S.G.J. Heijman, W.G.J. van der Meer, Effect of spacer configuration on hydraulic conditions using PIV, Separ. Purif. Technol. 199 (2018) 9–19.
[3] S.S. Bucs, A.I. Radu, V. Lavric, J.S. Vrouwenvelder, C. Picioreanu, Effect of different commercial feed spacers on biofouling of reverse osmosis membrane systems: a numerical study, Desalination 343 (2014) 26–37.
[4] A.I. Radu, J.S. Vrouwenvelder, M.C.M. van Loosdrecht, C. Picioreanu, Modeling the effect of biofilm formation on reverse osmosis performance: flux, feed channel pressure drop and solute passage, J. Membr. Sci. 365 (2010) 1–15.
[5] J.S. Vrouwenvelder, D.A. Graf von der Schulenburg, J.C. Kruithof, M.L. Johns, M.C.M. van Loosdrecht, Biofouling of spiral-wound nanofiltration and reverse osmosis membranes: a feed spacer problem, Water Res. 43 (2009) 583–594.
[6] J.S. Vrouwenvelder, J.A.M. van Paassen, J.M.C. van Agtmaal, M.C.M. van Loosdrecht, J.C. Kruithof, A critical flux to avoid biofouling of spiral wound nanofiltration and reverse osmosis membranes: fact or fiction? J. Membr. Sci. 326 (2009) 36–44.
[7] L. Fortunato, S. Bucs, R.V. Linares, C. Cali, J.S. Vrouwenvelder, T. Leiknes, Spatially-resolved in-situ quantification of biofouling using optical coherence tomography (OCT) and 3D image analysis in a spacer filled channel, J. Membr. Sci. 524 (2017) 673–681.
[8] A.I. Radu, M.S.H. van Steen, J.S. Vrouwenvelder, M.C.M. van Loosdrecht, C. Picioreanu, Spacer geometry and particle deposition in spiral wound membrane feed channels, Water Res. 64 (2014) 160–176.
[9] M. Wagner, B. Manz, F. Volke, T.R. Neu, H. Horn, Online assessment of biofilm development, sloughing and forced detachment in tube reactor by means of magnetic resonance microscopy, Biotechnol. Bioeng. 107 (2010) 172–181.
[10] C. Picioreanu, J.S. Vrouwenvelder, M.C.M. van Loosdrecht, Three-dimensional modeling of biofouling and fluid dynamics in feed spacer channels of membrane devices, J. Membr. Sci. 345 (2009) 340–354.
[11] S. Kerdi, A. Qamar, A. Alpatova, N. Ghaffour, An in-situ technique for the direct structural characterization of biofouling in membrane filtration, J. Membr. Sci. 583 (2019) 81–92.
[12] G. Belfort, G.A. Guter, An experimental study of electrodialysis hydrodynamics, Desalination 10 (1972) 221–262.
[13] P. Feron, G.S. Solt, The influence of separators on hydrodynamics and mass transfer in narrow cells: flow visualisation, Desalination 84 (1991) 137–152.
[14] O. Kuroda, S. Takahashi, M. Nomura, Characteristics of flow and mass transfer rate in an electrodialyzer compartment including spacer, Desalination 46 (1983) 225–232.
[15] G. Schock, A. Miquel, Mass transfer and pressure loss in spiral wound modules, Desalination 64 (1987) 339–352.
[16] Y. Winograd, A. Solan, M. Toren, Mass transfer in narrow channels in the presence of turbulence promoters, Desalination 13 (1973) 171–186.
[17] C.C. Zimmerer, V. Kottke, Effects of spacer geometry on pressure drop, mass transfer, mixing behavior, and residence time distribution, Desalination 104 (1996) 129–134.
[18] J. Fárková, The pressure drop in membrane module with spacers, J. Membr. Sci. 64 (1991) 103–111.
[19] Z. Cao, D.E. Wiley, A.G. Fane, CFD simulations of net-type turbulence promoters in a narrow channel, J. Membr. Sci. 185 (2001) 157–176.
[20] P.R. Neal, H. Li, A.G. Fane, D.E. Wiley, The effect of filament orientation on critical flux and particle deposition in spacer-filled channels, J. Membr. Sci. 214 (2003) 165–178.
[21] J. Schwinge, D.E. Wiley, A.G. Fane, Novel spacer design improves observed flux, J. Membr. Sci. 229 (2004) 53–61.
[22] J. Schwinge, D.E. Wiley, D.F. Fletcher, A CFD study of unsteady flow in narrow spacer-filled channels for spiral-wound membrane modules, Desalination 146 (2002) 195–201.
[23] D.E. Wiley, D.F. Fletcher, Computational fluid dynamics modelling of flow and permeation for pressure-driven membrane processes, Desalination 145 (2002) 183–186.
[24] D.E. Wiley, D.F. Fletcher, Techniques for computational fluid dynamics modelling of flow in membrane channels, J. Membr. Sci. 211 (2003) 127–137.
[25] N. Sreedhar, N. Thomas, O. Al-Ketan, R. Rowshan, H. Hernandez, R.K. Abu Al-Rub, H.A. Arafat, 3D printed feed spacers based on triply periodic minimal surfaces for flux enhancement and biofouling mitigation in RO and UF, Desalination 425 (2018) 12–21.
[26] G.A. Fimbres-Weihs, D.E. Wiley, Numerical study of mass transfer in three-dimensional spacer-filled narrow channels with steady flow, J. Membr. Sci. 306 (2007) 228–243.
[27] G.A. Fimbres-Weihs, D.E. Wiley, D.F. Fletcher, Unsteady flows with mass transfer in narrow zigzag spacer-filled Channels: a numerical study, Ind. Eng. Chem. Res. 45 (2006) 6594–6603.
[28] C.P. Koutsou, S.G. Yiantsios, A.J. Karabelas, Numerical simulation of the flow in a plane-channel containing a periodic array of cylindrical turbulence promoters, J. Membr. Sci. 231 (2004) 81–90.
[29] C.P. Koutsou, S.G. Yiantsios, A.J. Karabelas, A numerical and experimental study of mass transfer in spacer-filled channels: effects of spacer geometrical characteristics and Schmidt number, J. Membr. Sci. 326 (2009) 234–251.
[30] A.R. Da Costa, A.G. Fane, C.J.D. Fell, A.C.M. Franken, Optimal channel spacer design for ultrafiltration, J. Membr. Sci. 62 (1991) 275–291.
[31] A.R. Da Costa, A.G. Fane, Net-type spacers: effect of configuration on fluid flow path and ultrafiltration flux, Ind. Eng. Chem. Res. 33 (1994) 1845–1851.
[32] A.Q. Sarah Kerdi, Johannes S. Vrouwenvelder, Noreddine Ghaffour, Fouling resilient perforated feed spacers for membrane filtration, Water Res. 140 (2018) 211–219.
[33] J.S. Vrouwenvelder, S.M. Bakker, L.P. Wessels, J.A.M. van Paassen, The Membrane Fouling Simulator as a new tool for biofouling control of spiral-wound membranes, Desalination 204 (2007) 170–174.
[34] B. Manz, F. Volke, D. Goll, H. Horn, Measuring local flow velocities and biofilm structure in biofilm systems with Magnetic Resonance Imaging (MRI), Biotechnol. Bioeng. 84 (2003) 424–432.
[35] Y. Gao, S. Haavisto, C.Y. Tang, J. Salmela, W. Li, Characterization of fluid dynamics in spacer-filled channels for membrane filtration using Doppler optical coherence tomography, J. Membr. Sci. 448 (2013) 198–208.
[36] S.S. Bucs, R. Valladares Linares, J.O. Marston, A.I. Radu, J.S. Vrouwenvelder, C. Picioreanu, Experimental and numerical characterization of the water flow in spacer-filled channels of spiral-wound membranes, Water Res. 87 (2015) 299–310.
[37] M. Gimmelshtein, R. Semiat, Investigation of flow next to membrane walls, J. Membr. Sci. 264 (2005) 137–150.
[38] J. Schwinge, D.E. Wiley, D.F. Fletcher, Simulation of the flow around spacer filaments between narrow channel walls. 1, Hydrodyn. Ind. Eng. Chem. Res. 41 (2002) 2977–2987.
[39] J. Schwinge, D.E. Wiley, D.F. Fletcher, Simulation of the flow around spacer filaments between channel walls. 2, Mass Transf. Enhance. Ind. Eng. Chem. Res. 41 (2002) 4879–4888.
[40] J. Schwinge, D.E. Wiley, D.F. Fletcher, Simulation of unsteady flow and vortex shedding for narrow spacer-filled channels, Ind. Eng. Chem. Res. 42 (2003) 4962–4977.
[41] C.P. Koutsou, S.G. Yiantsios, A.J. Karabelas, Direct numerical simulation of flow in spacer-filled channels: effect of spacer geometrical characteristics, J. Membr. Sci. 291 (2007) 53–69.
[42] Y.-D. Kim, L. Francis, J.-G. Lee, M.-G. Ham, N. Ghaffour, Effect of non-woven net spacer on a direct contact membrane distillation performance: experimental and theoretical studies, J. Membr. Sci. 564 (2018) 193–203.
[43] V.A. Haaksman, A. Siddiqui, C. Schellenberg, J. Kidwell, J.S. Vrouwenvelder, C. Picioreanu, Characterization of feed channel spacer performance using geometries obtained by X-ray computed tomography, J. Membr. Sci. 522 (2017) 124–139.
[44] N. Horstmeyer, T. Lippert, D. Schön, F. Schlederer, C. Picioreanu, K. Achterhold, F. Pfeiffer, J.E. Drewes, CT scanning of membrane feed spacers – impact of spacer model accuracy on hydrodynamic and solute transport modeling in membrane feed channels, J. Membr. Sci. 564 (2018) 133–145.
[45] A. Pages, M. Sermesant, P. Frey, Generation of computational meshes from MRI and CT-scan data, ESAIM Proc. 14 (2005) 213–223.
[46] D.C. Wilcox, Turbulence Modeling for CFD D C W Industries, third ed., (2006).
[47] J.C. Vassilicos, Kolmogorov's contributions to the physical and geometrical understanding of small-scale turbulence and recent developments, Proc. R. Soc. A Math. Phys. Eng. Sci. 434 (1991) 183–210.
[48] G.A. Fimbres-Weihs, D.E. Wiley, Review of 3D CFD modeling of flow and mass

transfer in narrow spacer-filled channels in membrane modules, Chem. Eng. Process: Process Intensif. 49 (2010) 759–781.
[49] P. Moin, K. Mahesh, Direct numerical simulation: a tool in turbulence research, Annu. Rev. Fluid Mech. 30 (1998) 539–578.
[50] M.S. Mohammad, Experimental and numerical study of flow within spacer-filled channels, Mechanical and Materials Engineering, Queen's University, 2014.
[51] F. Li, G.W. Meindersma, A.B. de Haan, T. Reith, Optimization of non-woven spacers by CFD and validation by experiments, Desalination 146 (2002) 209–212.
[52] F. Li, W. Meindersma, A.B. de Haan, T. Reith, Optimization of commercial net spacers in spiral wound membrane modules, J. Membr. Sci. 208 (2002) 289–302.
[53] ANSYS Theory Guide, Southpointe, 275 Technology Drive, Canonsburg, PA 15317, (Version 17, 2016).
[54] W. Zhang, W. Cheng, W. Gao, A. Qamar, R. Samtaney, Geometrical effects on the airfoil flow separation and transition, Comput. Fluids 116 (2015) 60–73.
[55] ANSYS Meshing User's Guide, Southpointe, 275 Technology Drive, Canonsburg, PA 15317, (Version 17, 2016).
[56] K.S. Laboratory, SHAHEEN II user guide, KAUST, 2016 https://www.hpc.kaust.edu.sa/content/shaheen-ii.
[57] W.L. Oberkampf, T.G. Trucano, Verification and validation in computational fluid dynamics, Prog. Aerosp. Sci. 38 (2002) 209–272.
[58] H.B. Henninger, S.P. Reese, A.E. Anderson, J.A. Weiss, Validation of computational models in biomechanics, Proc. Inst. Mech. Eng. H J. Eng. Med. 224 (2009) 801–812.
[59] D.P. Hart, PIV error correction, Exp. Fluid 29 (2000) 13–22.
[60] Y. Zhang, K. Liu, H. Xian, X. Du, A review of methods for vortex identification in hydroturbines, Renew. Sustain. Energy Rev. 81 (2018) 1269–1285.
[61] J.H. Chen, W.G. Pritchard, S.J. Tavener, Bifurcation for flow past a cylinder between parallel planes, J. Fluid Mech. 284 (1995) 23–41.
[62] A. Qamar, R. Samtaney, J.L. Bull, Pulsatility role in cylinder flow dynamics at low Reynolds number, Phys. Fluids 24 (2012) 081701.
[63] M. Sahu, P. Singh, S.S. Mahapatra, K.K. Khatua, Prediction of entrance length for low Reynolds number flow in pipe using neuro-fuzzy inference system, Expert Syst. Appl. 39 (2012) 4545–4557.
[64] K.R. Rao, D.N. Kim, J.-J. Hwang, Fast Fourier Transform - Algorithms and Applications, Incorporated Springer Publishing Company, 2010.
[65] A. Qamar, N. Hasan, S. Sanghi, A new spatial discretization strategy of the convective flux term for the hyperbolic conservation laws, Eng. Appl. Comput. Fluid Mech. 4 (2010) 593–611.
[66] N. Ghaffour, R. Jassim, T. Khir, Flux enhancement by using helical baffles in ultrafiltration of suspended solids, Desalination 167 (2004) 201–207.
[67] S. Lecuyer, R. Rusconi, Y. Shen, A. Forsyth, H. Vlamakis, R. Kolter, H.A. Stone, Shear stress increases the residence time of adhesion of Pseudomonas aeruginosa, Biophys. J. 100 (2011) 341–350.
[68] S. Soukane, M.W. Naceur, L. Francis, A. Alsaadi, N. Ghaffour, Effect of feed flow pattern on the distribution of permeate fluxes in desalination by direct contact membrane distillation, Desalination 418 (2017) 43–59.